THE JOURNAL OF BIOLOGICAL CHEMISTRY VOL. 282, NO. 7, pp. 4859–4867, February 16, 2007
Printed in the U.S.A.

Characterization, Kinetics, and Crystal Structures of Fructose-1,6-bisphosphate Aldolase from the Human Parasite, *Giardia lamblia**

Received for publication, October 10, 2006, and in revised form, November 28, 2006 Published, JBC Papers in Press, December 13, 2006, DOI 10.1074/jbc.M609534200

Andrey Galkin‡, Liudmila Kulakova‡, Eugene Melamud‡, Ling Li§, Chun Wu§[1], Patrick Mariano§, Debra Dunaway-Mariano§, Theodore E. Nash¶, and Osnat Herzberg‡[2]

From the ‡Center for Advanced Research in Biotechnology, University of Maryland Biotechnology Institute, Rockville, Maryland 20850, the §Department of Chemistry, University of New Mexico, Albuquerque, New Mexico 87131, and ¶Laboratory of Parasitic Diseases, NIAID, National Institutes of Health, Bethesda, Maryland 20892

Class I and class II fructose-1,6-bisphosphate aldolases (FBPA), glycolytic pathway enzymes, exhibit no amino acid sequence homology and utilize two different catalytic mechanisms. The mammalian class I FBPA employs a Schiff base mechanism, whereas the human parasitic protozoan *Giardia lamblia* class II FBPA is a zinc-dependent enzyme. In this study, we have explored the potential exploitation of the *Giardia* FBPA as a drug target. First, synthesis of FBPA was demonstrated in *Giardia* trophozoites by using an antibody-based fluorescence assay. Second, inhibition of FBPA gene transcription in *Giardia* trophozoites suggested that the enzyme is necessary for the survival of the organism under optimal laboratory growth conditions. Third, two crystal structures of FBPA in complex with the transition state analog phosphoglycolohydroxamate (PGH) show that the enzyme is homodimeric and that its active site contains a zinc ion. In one crystal form, each subunit contains PGH, which is coordinated to the zinc ion through the hydroxamic acid hydroxyl and carbonyl oxygen atoms. The second crystal form contains PGH only in one subunit and the active site of the second subunit is unoccupied. Inspection of the two states of the enzyme revealed that it undergoes a conformational transition upon ligand binding. The enzyme cleaves D-fructose-1,6-bisphosphate but not D-tagatose-1,6-bisphosphate, which is a tight binding competitive inhibitor. The essential role of the active site residue Asp-83 in catalysis was demonstrated by amino acid replacement. Determinants of catalysis and substrate recognition, derived from comparison of the *G. lamblia* FBPA structure with *Escherichia coli* FBPA and with a closely related enzyme, *E. coli* tagatose-1,6-bisphosphate aldolase (TBPA), are described.

Giardia lamblia, a flagellated protozoan, is the most common disease-causing parasite in developed countries. *G. lamblia* is also responsible for the most frequently diagnosed infective disease in developing countries (for a recent review see Ref. 1). The manifestations of giardiasis disease range from severe diarrhea, weight loss, vomiting, and malnutrition to asymptomatic carriage. *G. lamblia* is an ancient eukaryote. Its cellular biology and biochemistry are not well defined, and as a result, there is much to learn about its survival and adaptation tactics. Currently, giardiasis is treated by using metronidazole or tinidazole. Although the cure rates using tinidazole and metronidazole drug therapy are presently in excess of 60%, it is clear that alternative drug treatments are needed. Both drugs produce undesirable side effects, and increasing resistance to drug regimes presents a potential problem (2–6). Recurrence is also a problem, with frequency reported to be as high as 90% (4). In pursuit of alternative drug therapies, we have examined the recently reported *G. lamblia* genome sequence (7) in order to uncover genes that encode optimal targets.

This analysis has led to our interest in the *G. lamblia* fructose-1,6-bisphosphate aldolase (EC 4.1.2.13) (*gl*FBPA),[3] an enzyme that catalyzes the reversible cleavage of D-fructose 1,6-bisphosphate (FBP) to dihydroxyacetone phosphate (DHAP) and D-glyceraldehyde 3-phosphate (G3P) (Fig. 1*A*). This process is a key step in the classical Embden-Meyerhof-Parnas glycolytic pathway. Because *G. lamblia* lacks mitochondria as well as the components of oxidative phosphorylation, glucose degradation via glycolysis serves as its major source of ATP (8–10). We envisioned that selective inhibition of FBPA might disrupt the functioning of the glycolytic pathway and thereby hinder survival of *G. lamblia* within its human host. Unlike the mammalian FBPA, which is a class I aldolase, *gl*FBPA belongs to the class II family (11). The former FBPA uses an active site lysine residue to activate the substrate for C(3)–C(4) bond cleavage via Schiff base formation (Fig. 2). In con-

---

* This work was supported by National Institutes of Health Grant RO1 AI059733. The costs of publication of this article were defrayed in part by the payment of page charges. This article must therefore be hereby marked "*advertisement*" in accordance with 18 U.S.C. Section 1734 solely to indicate this fact.

The atomic coordinates and structure factors (code 2ISV, 2ISW) have been deposited in the Protein Data Bank, Research Collaboratory for Structural Bioinformatics, Rutgers University, New Brunswick, NJ (http://www.rcsb.org/).

[1] Present address: Chemistry Dept., Division of Natural Sciences, Mount Marty College, Yankton, SD 57078.

[2] To whom correspondence should be addressed: Center for Advanced Research in Biotechnology, 9600 Gudelsky Dr., Rockville MD 20850. Tel.: 240-314-6245; Fax: 240-314-6255; E-mail: osnat@carb.nist.gov.

[3] The abbreviations used are: *gl*FBPA, *Giardia* FBPA; FBPA, fructose-1,6-bisphosphate aldolase; *ec*TBPA, *E. coli* tagatose-1,6-bisphosphate aldolase; *ec*FBPA, *E. coli* FBPA; PGH, phosphoglycolohydroxamate; FBP, D-fructose-1,6-bisphosphate; TBP, D-tagatose-1,6-bisphosphate; DHAP, dihydroxyacetone phosphate; G3P, D-glyceraldehyde 3-phosphate; MES, 2-(*N*-morpholino)ethanesulfonic acid; BisTris, 2,2-bis(hydroxymethyl)-2,2′,2-nitrilotriethanol; TAPS, *N*-tris(hydroxymethyl)methyl-3-aminopropanesulfonic acid; CHES, *N*-cyclohexyl-2-aminoethanesulfonic acid; CAPS, *N*-cyclohexyl-3-aminopropanesulfonic acid; PDB, Protein Data Bank; r.m.s.d., root-mean-square deviation; IMCA-CAT, Industrial Macromolecular Crystallography Association-Collaborative Access Team.

trast, class II FBPAs use a Zn^{2+} cofactor to coordinate both the C(2) carbonyl and C(3) hydroxyl oxygens of the substrate, consequently stabilizing the enediolate intermediate formed by C(3)–C(4) bond cleavage (12, 13) (Fig. 2). Importantly, our genomic sequence analysis indicates that FBPA is the only *Giardia* class II aldolase and that the *Giardia* genome does not encode a class I aldolase.

The mechanistically dissimilar class I and II aldolases do not share significant amino acid sequence homology. The evolutionary significance of this finding has been discussed previously (12, 14). The divergence in class I and II aldolase structures and catalytic mechanisms suggests a novel strategy for the design of drugs that operate by selectively inhibiting the activity of FBPA in the *G. lamblia* parasite but not in mammalian FBPA.

To date, the most thoroughly characterized class II FBPA is the enzyme from *Escherichia coli* (*ec*FBPA). Crystal structures have been determined for apo-*ec*FBPA and for the enzyme complexed with a transition state analog, phosphoglycolohydroxamate (PGH) (Fig. 1*B*) (15, 16). The structures, together with kinetic properties of active site site-directed mutants, have provided significant insight into the class II FBPA catalytic mechanism (17–19). The class II FBPA adopts an $(\alpha/\beta)_8$-barrel fold that supports a catalytic site at the C-terminal end of the barrel. The Zn^{2+} coordinates the imidazole rings of His-110, His-226, and His-264 located at this site and with the C(2)=O and C(3) hydroxyl oxygen atoms of the substrate. In this manner, the coordinated Zn^{2+} serves as an electron sink, stabilizing the enolate anion intermediate (17, 18) (Fig. 2).

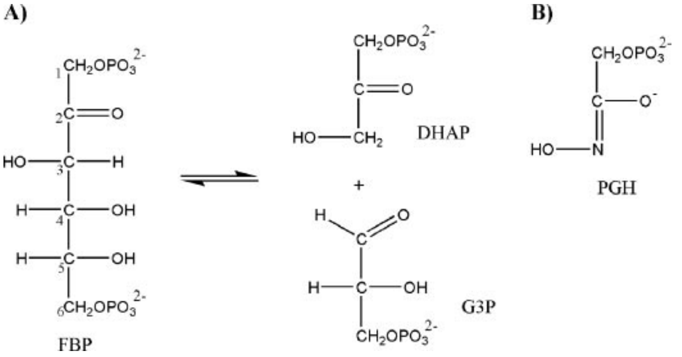

FIGURE 1. *A*, reaction catalyzed by FBPA. *B*, FBPA inhibitor, PGH, mimicking the DHAP ene-diolate transition-state intermediate.

*ec*FBPA exhibits very low activity toward the C(4) epimer of FBP, D-tagatose-1,6-bisphosphate (TBP), which is also a cellular metabolite (18). Because deprotonation of the C(4) hydroxyl initiates C(3)–C(4) bond cleavage (Fig. 2), it is likely that the FBP-TBP selectivity is the consequence of the orientation of the substrate relative to the general base. TBP is specifically targeted for cleavage by the *E. coli* D-tagatose-1,6-bisphosphate aldolase (*ec*TBPA), another class II aldolase. The crystal structures of *ec*FBPA (15, 16) and *ec*TBPA (20) are similar, yet the mechanism for substrate (*i.e.* stereoisomer) discrimination is not apparent from a comparison of the respective active sites. It is curious that the *G. lamblia* aldolase II shares greater sequence homology with the *ec*TBPA than it does with the *ec*FBPA.

In this study, we describe our studies of *gl*FBPA, which is the first example of a eukaryotic class II aldolase to be characterized. The x-ray structure of the enzyme in complex with the Zn^{2+} cofactor and PGH is reported, as are the kinetic constants for *gl*FBPA catalysis of FBP and TBP cleavage. Finally, the essential role of the active site residue, Asp-83, in catalysis was confirmed by amino acid replacement and kinetic analysis of the mutant enzyme.

MATERIALS AND METHODS

Protein Cloning, Expression, and Purification—The trophozoites of the *G. lamblia* isolate WB, clone 1267, were grown as described previously (21). The genomic DNA preparation was performed with the DNA Stat kit (Stratagene).

The PCR product was introduced into the pET100/D-TOPO expression vector (Invitrogen). Recombinant plasmids were isolated from the *E. coli* TOP10 strain (pET100/FBPAn).

For protein production, the *E. coli* strain BL21(DE3)Star was transformed with the pET100/FBPAn recombinant plasmid. Cells were grown in LB media at 30 °C to A_{600} = 0.5, when isopropyl 1-thio-β-D-galactopyranoside (0.1 mM) was added. After 3 h, cells were collected by centrifugation and suspended in 50 mM Tris-HCl (pH 8.5) and 10% glycerol. The cells were broken by passage through a French press. The soluble fraction was applied onto an anion exchange column, Sepharose Q (Amersham Biosciences). FBPA was eluted using a linear gradient of 0–0.5 M NaCl in 50 mM Tris-HCl (pH 8.5) and 5% glycerol. Concentrated protein fractions were applied onto a preparative gel filtration column, Sephacryl 100 (Amersham Biosciences). The remaining minor impurities were removed by using a hydrophobic column, phenyl-Sepharose (Amer-

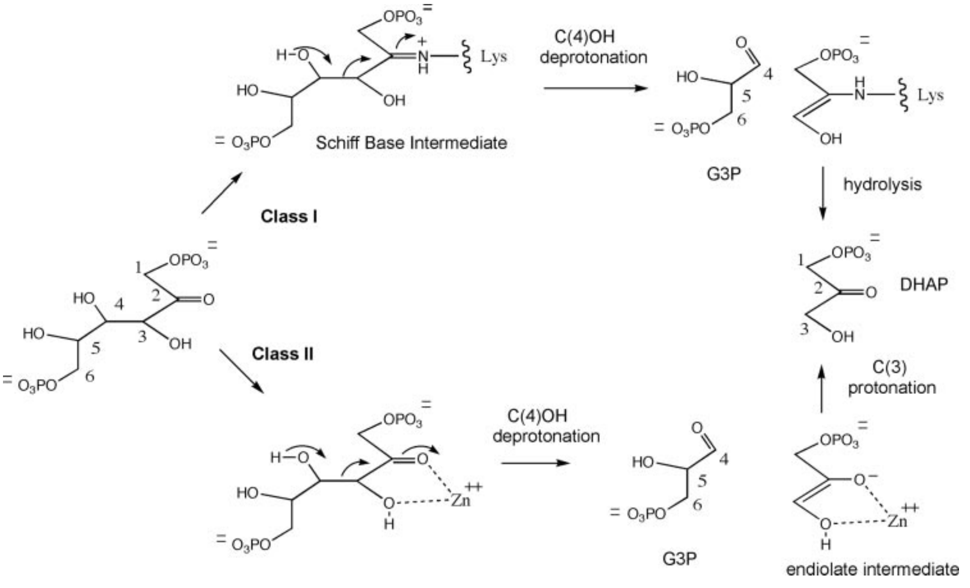

FIGURE 2. **The catalytic mechanism of class I and class II FBPA.**

sham Biosciences). The protein was eluted with a linear ammonium sulfate gradient (1.5-0 M), dialyzed against 20 mM Tris-HCl (pH 8.0) and 50 mM NaCl solution, concentrated to 12 mg/ml, flash-cooled in liquid nitrogen, and stored at −80 °C.

Preparation of D83A glFBPA Mutant—The QuickChange mutagenesis kit (Stratagene) was used in combination with the pET100/FBPAn plasmid template and the *E. coli* strain BL21(DE3)Star cell line. The mutant sequence was confirmed by DNA sequencing. Homogeneous D83A *gl*FBPA was prepared using the same procedure described above for the wild-type enzyme.

Steady-state Kinetic Constant Determination—Initial velocities were measured at 25 °C using 1-ml reaction solutions containing *gl*FBPA (0.016 μM), 200 μM NADH, 5 units of triose-phosphate isomerase, 2 units of glycerol-3-phosphate dehydrogenase, and varying concentrations of FBP (K_m, 0.5–10) in 50 mM K^+HEPES (pH 7.5). The absorbance of the reaction solution was monitored at 340 nm ($\epsilon = 6.2$ mM^{-1} cm^{-1}). For D83A *gl*FBPA, a single velocity measurement was made using 170 μM protein and 2 mM FBP and monitoring the solution absorbance at 340 nm for 3 h. The velocity of wild-type *gl*FBPA-catalyzed cleavage of TBP (supplied by Dr. Wolf-Dieter Fessner of Technische Universität, Darmstadt, Germany) was similarly measured using 3.5 mM TBP tetra(cyclohexylammonium) salt and 74 μM *gl*FBPA.

To determine the kinetic constants, the initial velocity data were fitted to Equation 1 with KinetAsystI (IntelliKinetics, State College, PA),

$$V_0 = V_{\max}[S]/(K_m + [S]) \qquad \text{(Eq. 1)}$$

where [S] is the substrate concentration; V_0 is the initial velocity; $V_{\max}$ is the maximum velocity; and K_m is the Michaelis-Menten constant for the substrate. The k_{cat} value was calculated from $V_{\max}$ and the enzyme concentration [*E*] (determined employing the Bradford method (22)) using the equation $k_{cat} = V_{\max}/[E]$.

The competitive inhibition constants (K_i) of PGH (synthesized as the cyclohexylammonium chloride salt using a previously published protocol (23)) and TBP were determined by measuring the initial velocity of the above reactions at 0, 50, 100, and 150 nM PGH ([I]), and 6 and 20 μM TBP, and fitting the data to Equation 2 with KinetAsystI.

$$V_0 = V_{\max}[S]/(K_m(1 + (I/K_i)) + [S]) \qquad \text{(Eq. 2)}$$

pH Rate Profile Determination—The initial velocity data were measured as a function of the pH by using the following (50 mM) buffer at the indicated pH values: MES and potassium acetate (4.0–5.0), MES (5.5), BisTris (6.0–6.5), HEPES (7.0–8.0), TAPS (8.5), CHES (9.0–9.5), and CAPS (10.0–10.5). The k_{cat} and k_{cat}/K_m values were fitted to Equations 3 and 4, respectively, using the computer program KinetAsyst,

$$\log Y = \log(C/(1 + [H]/K_a + K_b/[H])) \qquad \text{(Eq. 3)}$$

$$\log Y = \log(C/(1 + [H]/K_a + K_b/[H] + [H]^2/K_aK_b)) \qquad \text{(Eq. 4)}$$

where *Y* is k_{cat} or k_{cat}/K_m; [H] is the hydrogen ion concentration; *C* is the pH-independent value of k_{cat} or k_{cat}/K_m; K_a is the acid dissociation constant; and K_b is the base dissociation constant.

Analytical Size Exclusion Chromatography—For estimation of the oligomeric state of the protein, analytical size exclusion chromatography was performed using a Superdex-200 HR 10/30 column (Amersham Biosciences). Runs were performed at a flow rate of 0.4 ml/min with 50 mM Tris-HCl (pH 7.5) and 0.1 M NaCl serving as eluant.

Polyclonal Antibody Production and Immunofluorescence Assay—Polyclonal antibodies against purified *gl*FBPA were produced in BALB/c mice (Spring Valley Laboratories, Inc.). Fluorescein isothiocyanate-conjugated, affinity-purified goat anti-mouse immunoglobulin was used as the secondary antibody, and the control consisted of omission of the primary antibody. The specimens were examined with an Axioplan fluorescence microscope (Carl Zeiss, Thornwood, NY).

Functional Knock-out Experiments of the FBPA Gene in G. lamblia—The FBPA gene was inserted into the plasmid pdsRNA between two opposite tetracycline-inducible Ras-related nuclear GTP-binding protein (*ran*) promoters, and knock-out experiments were carried out as described previously (24).

Crystallization and Data Collection—Crystals were grown at room temperature in hanging drops using the vapor diffusion method. The protein solution was mixed with an equal volume of mother liquor containing 18–23% polyethylene glycol monomethyl ether 2000, 0.1 M Tris-HCl (pH 8.8), and 0.2 M $MgCl_2$. Hexagonal and orthorhombic crystals were obtained from protein solutions that were incubated on ice for 30 min with 20 mM PGH. The hexagonal crystals diffracted x-rays to a resolution of 2.3 Å. The orthorhombic crystals appeared within 4–8 weeks, and they diffracted x-rays to a resolution of 1.75 Å. For data collection, the crystals were transferred to solutions containing mother liquor and 20% glycerol and flash-cooled with liquid propane cooled in liquid nitrogen.

Diffraction data were acquired at the Industrial Macromolecular Crystallography Association-Collaborative Access Team (IMCA-CAT) 17-ID/BM beamlines at the Advanced Photon Source (Argonne National Laboratory, Argonne, IL). For data acquisition, the IMCA-CAT beamline was equipped with a Q210 CCD detector (ADSC, San Diego) or MARCCD 165 detector (Marresearch, Norderstedt, Germany). Data processing was carried out using HKL (25). The asymmetric unit of either crystal form contains two protein molecules. The statistics of data collection are provided in Table 1.

Structure Determination and Refinement—The structure of *gl*FBPA was determined by molecular replacement using the program CNS (26) and the 2.3 Å diffraction data from the hexagonal crystal form. The search model was built based on *E. coli* tagatose-1,6-bisphosphate aldolase (*ec*TBPA), which shares 38% amino acid sequence identity with *gl*FBPA (PDB entry 1GVF (20)). Structure refinement was carried out using the CNS program (26). The orthorhombic crystal form structure was obtained by molecular replacement using a partially refined structure of the hexagonal crystal form as the search model. The models were inspected and modified on a graphics work station using the program O (27). Water molecules were added to the model based on the $F_o - F_c$ difference Fourier electron

TABLE 1
X-ray data collection and refinement statistics

Crystal form	Hexagonal	Orthorhombic
Data collection		
Space group	$P6_1$	$C222_1$
Cell dimension		
a, *b*, c (Å)	62.4, 62.4, 319.9	90.0, 90.1, 166.1
Resolution range (Å)	30-2.3	30-1.75
No. of observations	127,478	334,755
No. of unique reflections	28,450	56,981
Completeness (%)[a]	91.6 (77.9)	83.6 (75.2)
R_{merge}[b]	0.037 (0.116)	0.059 (0.492)
Refinement statistics		
No. of reflections	28,450	56,981
No. of residues	605	595
No. of water molecules	368	440
R_{cryst}[c]	0.199	0.186
R_{free}[d]	0.261	0.225
Root mean square deviation		
Bonds (Å)	0.018	0.016
Angles (°)	2.0	1.8
Average *B* factor (Å^2)	51.3	32.9
Ramachandran plot (%)		
Most favored	88.6	92.9
Allowed	11.0	6.7
Disallowed (Met-59)	0.4	0.4

[a] The values in parentheses are for the highest resolution shell.

[b] $R_{\mathrm{merge}} = \Sigma_{hkl}((\Sigma_j|I_j - \langle I\rangle|)/\Sigma_j|I_j|)$, for equivalent reflections.

[c] $R_{\mathrm{cryst}} = \Sigma_{hkl}||F_o| - |F_c||/\Sigma_{hkl}|F_o|$, where F_o and F_c are the observed and calculated structure factors, respectively.

[d] R_{free} is computed for 5% of reflections that were randomly selected and omitted from the refinement.

density map (where F_o and F_c are the observed and calculated structure factors, respectively), using peaks with density $\geq 3\sigma$ as the acceptance criteria. Refinement statistics are provided in Table 1. PROCHECK was used for analysis of geometry (28), QUANTA for molecular modeling and structural alignment (Molecular Simulations Inc.), and PyMOL for depiction of the structures (29).

Zinc Ion Detection—The presence of zinc in the crystals was confirmed by x-ray fluorescence at the zinc absorption edge energy measured at the IMCA-CAT beam line 17-ID. Data were measured using a Bicron fluorescent detector while increasing the monochromator energy in small steps from 9600 to 9900 eV.

Modeling the Enzyme-Substrate Complex—The FBP coordinates, taken from the crystal structure of the class I rabbit liver FBPA (PDB entry 1FDJ), were used to place FBP in the active site of *gl*FBPA. The DHAP portion of FBP was placed manually in a position equivalent to that of PGH. The positioning of the G3P portion of FBP was based on information from site-directed mutagenesis experiments, as detailed under "Results and Discussion." The final model was optimized by energy minimization of the docked FBP and residues surrounding the G3P portion of the substrate using the program CNS.

RESULTS AND DISCUSSION

Identification of glFBPA as Potential Drug Target—*gl*FBPA was selected together with a number of other potential *Giardia* drug target candidates based on genome-scale sequence analysis. The criteria for selection were as follows: 1) the likely absolute requirement for *Giardia* survival, and 2) either the absence in the human genome or sufficient sequence divergence from the human counterpart (30, 31).

The sequencing of the *G. lamblia* genome is nearly complete (7). At the time of target selection, the list of *Saccharomyces cerevisiae* essential genes included 878 genes (32), comprising the most comprehensive cell viability data available for a eukaryotic organism. BlastP sequence analysis (33) of this list against the genome sequence of *G. lamblia* yielded 332 non-transmembrane proteins larger than 100 amino acid residues and that exhibit sequence homology to yeast essential genes with *E* score $<10^{-3}$.

The gene set was compared with the human genome data base (www.ncbi.nlm.nih.gov/genome/guide/human). One of the promising candidates that arose from this analysis was the gene encoding class II FBPA. In this context, it is noteworthy that *Plasmodium falciparum* and *Trypanosoma brucei* aldolases have been proposed as anti-malarial and anti-trypanosomal drug targets even though they belong to the class I enzymes and thus are closely related to the human enzyme (34, 35).

Expression and Characterization of glFBPA—To confirm that the gene encodes a true FBPA, the recombinant protein was expressed in *E. coli*. The theoretical mass of *gl*FBPA is 35,376.9 Da, which is consistent with the mobility of the protein on SDS-polyacrylamide gels. Gel filtration analysis indicated that the protein is predominantly a homodimer in solution. Homodimeric association was also observed for *ec*FBPA (16), in contrast to FBPAs from *Mycobacterium tuberculosis* (36) and *Thermus aquaticus* (37), and *ec*TBPA (20), which associate into homotetramers.

The steady-state kinetic constants for the *gl*FBPA-catalyzed cleavage of FBP at pH 7.5 and 25 °C in the absence of added Zn^{2+} are $k_{\mathrm{cat}} = 3.55 \pm 0.05\ \mathrm{s}^{-1}$, $K_m = 1.7 \pm 0.1\ \mu\mathrm{M}$, and $\mathrm{k}_{\mathrm{cat}}/K_m = 2.1 \times 10^6\ \mathrm{s}^{-1}\ \mathrm{M}^{-1}$. These values are within the range determined for other FBPAs (38).

Addition of Zn^{2+} to reaction solutions did not increase the catalytic rate. In fact, at a concentration in excess of 30 μM $ZnCl_2$, inhibition of catalysis was observed. This result suggested that the Zn^{2+} cofactor binds so tightly to *gl*FBPA that the protein isolated from the *E. coli* cells is completely Zn^{2+}-occupied. Moreover, attempts to remove the Zn^{2+} cofactor from *gl*FBPA by exhaustive dialysis against EDTA in Zn^{2+}-free buffer and then to restore catalytic activity by addition of Zn^{2+} were not successful. The dialyzed enzyme retained 50% of its original catalytic activity. The inclusion of $ZnCl_2$ in the activity assay did not restore the lost activity.

The pH dependence of *gl*FBPA catalysis was determined by measuring the k_{cat} and k_{cat}/K_m values as a function of reaction pH. Both pH rate profiles (Fig. 3) are bell-shaped, indicating that loss of activity occurs at acidic and basic pH. Therefore, all further kinetic determinations were carried out at pH 7.5 where FBPA displays optimal activity. The pH profiles were fitted to define the apparent pK_a values reported in Fig. 3 legend.

Class II FBPAs are known to be inhibited by PGH (23), an inhibitor that mimics the enediolate intermediate in the catalyzed reaction (Fig. 2). PGH is also known to inhibit triosephosphate isomerase (23), which promotes the ensuing step in the glycolytic pathway. Consequently, PGH has little potential for drug targeting of the *gl*FBPA within the human host. Nevertheless, PGH is an excellent probe for identification of the *gl*FBPA active site residues via x-ray crystal structure determi-

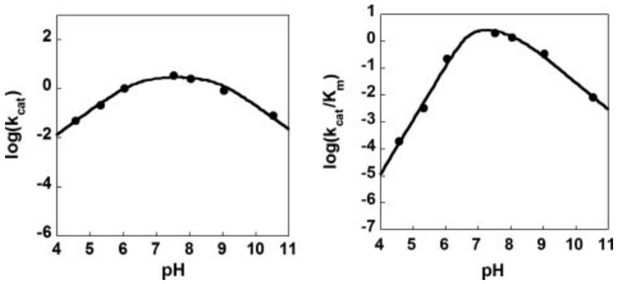

FIGURE 3. **Rate profiles that show the dependence of *gl*FBPA k_{cat} and k_{cat}/K_m values on the reaction pH.** See under "Materials and Methods" for details. The k_{cat} data were fitted to Equation 3 to define apparent pK_a values of 6.4 ± 0.1 and 8.8 ± 0.1. The k_{cat}/K_m data were fitted to Equation 4 to define apparent pK_a values of 6.0 ± 0.1 and 8.3 ± 0.4.

nation of the *gl*FBPA-Zn^{2+}-PGH complex. The binding affinity for PGH to *gl*FBPA is defined by $K_i = 37 \pm 2$ nM.

An analysis of *gl*FBPA sequence homologs suggests that the enzyme is more closely related to the *ec*TBPA (TBP is a C(4) epimer of FBP) than it is to the *ec*FBPA (38 and 23% sequence identity, respectively). This finding prompted the evaluation of the enzymatic activity of *gl*FBPA with TBP. The turnover rate for TBP is below the detection limit of the assay ($<5.5 \times 10^{-5}$ s^{-1}). The binding affinity for TBP to *gl*FBPA is reflected by the measured $K_i = 2.4 \pm 0.2$ μM.

In Vivo Enzyme Expression and Essentiality Test—Polyclonal antibodies raised against purified *gl*FBPA were used in conjunction with a fluorescein isothiocyanate-conjugated secondary antibody to detect the expression of FBPA within *G. lamblia* trophozoites (Fig. 4). No fluorescence was observed for the control experiment in which trophozoites were treated with the fluorescein isothiocyanate-conjugated secondary antibody in the absence of primary antibody. These results show that the trophozoites produce FBPA in a form that is recognized by antibodies raised against the native enzyme and that the protein is distributed throughout the organism.

The requirement of the enzyme for the *Giardia* parasite viability was examined by carrying out an *in vivo* experiment. This involved RNA interference/antisense RNA gene silencing techniques (39), recently adapted to *G. lamblia* trophozoites (24). Within 10 days after cultivation, trophozoites transfected with the silencing plasmid yielded no viable organisms even prior to induction by tetracycline. In control experiments that employed the nonessential gene encoding adaptor protein 1 involved in protein trafficking (24), viable trophozoites were observed after the transfection. The *ran* promoter can drive a low level of expression of the reporter gene even in the absence of tetracycline (40). Presumably, the "leakage" of the *ran* promoter enabled double-stranded RNA synthesis without induction. This triggered transcriptional inhibition and *gl*FBPA gene silencing. The results of the transcriptional inhibition experiments are consistent with the crucial role that the targeted *gl*FBPA plays in the *Giardia* glycolytic cycle as was suggested by genome analysis.

Overall Structure of glFBPA—The structure was determined by molecular replacement using the *ec*TBPA structure as a search model, which exhibits higher sequence identity to *gl*FBPA than *ec*FBPA (Table 2). Indeed, the *gl*FBPA structure more closely matches that of *ec*TBPA than *ec*FBPA despite the difference in substrate specificity of the former two enzymes (Table 2). This is opposite of what would be predicted based on substrate specificity alone.

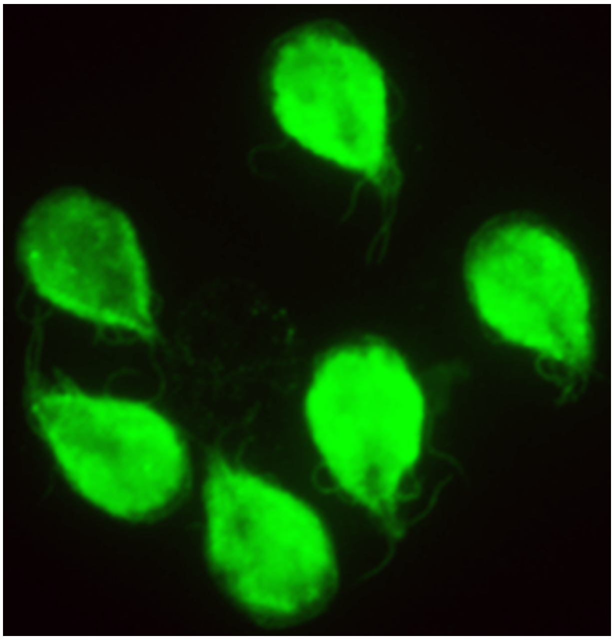

FIGURE 4. **Immunofluorescence assay of *G. lamblia* trophozoites reacting with polyclonal antibody against *gl*FBPA.** Fluorescein isothiocyanate-conjugated affinity-purified goat anti-mouse immunoglobulin was used as the secondary antibody.

Consistent with the results of the analytical gel filtration experiments, *gl*FBPA associates into a tightly packed dimer with approximate noncrystallographic 2-fold symmetry (Fig. 5). Each subunit (denoted A and B) folds into an $(\alpha/\beta)_8$ barrel as seen in structures of other bacterial class II aldolases (15, 16, 20, 37).

In the hexagonal crystal form, the two subunits are similar, as reflected by the low root-mean-square deviation (r.m.s.d.) of their α-carbon positions (0.3 Å) when the two molecules are superimposed. The active site of each subunit is occupied by Zn^{2+} and PGH. The first N-terminal residue of each molecule is not visible in the electron density map. In addition, no electron density is found to be associated with the surface residues 138–151, 181–189, and 323–324 in molecule A and 138–146, 184–188, and 323–324 in molecule B. These residues were omitted from the final model.

In the orthorhombic crystal form, the active site of one subunit (molecule A) is occupied by Zn^{2+} and PGH, whereas the active site of molecule B is not. Superposition of the two subunits yields an r.m.s.d. value between α-carbon positions of 0.8 Å, showing that the inhibitor-bound and unbound states have different conformations. The first N-terminal residue of each subunit is not visible in the electron density map. In addition, no electron density is associated with the surface residues 140–149, 186–189, and 323–324 in molecule A and 138–151, 176–190, 212–214, 235–236, and 324 in molecule B. These residues were omitted from the final model.

The relatively large r.m.s.d. value between the ligand-bound and ligand-free molecules is the consequence of the fact that two loops, spanning residues 174–194 and residues 227–237,

TABLE 2

Structural similarity between *gl*FBPA and other class II aldolases

PDB code	Protein	Z score	r.m.s.d.	No. aligned residues	Sequence identity (%)[a]
1JVF	*ec*TBPA-PGH complex	40	1.2	270	42
1B57	*ec*FBPA-PGH complex	32	1.9	269	24
1ZEN	*ec*FBPA	27	2.0	256	23

[a] The sequence identity corresponds to the structurally aligned residues.

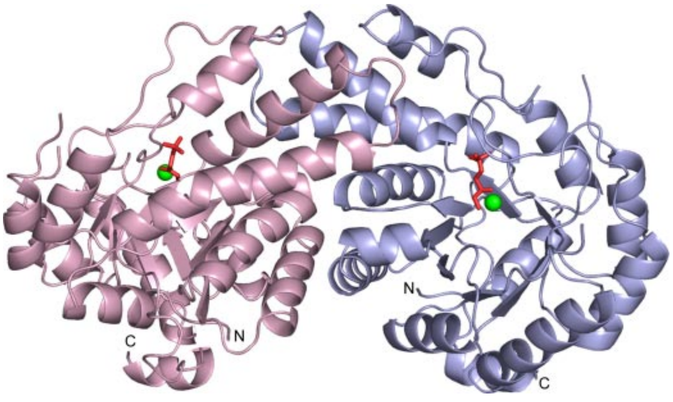

FIGURE 5. **Ribbon representation of the *gl*FBPA dimer in complex with PGH.** The catalytic site zinc ion is shown as a *green sphere*, and PGH is shown in a *red stick model.*

have undergone conformational transitions. The conformational changes do not appear to be the result of crystal packing. Most notably, the 174–194 loop is largely disordered in the unbound state, whereas, with the exception of residues 186–189, the loop conformation is defined in the bound state. Upon ligand binding, the two loops adopt ordered conformations, with several residues stationed to shape the active site cavity. Key residues on the 174–194 loop are involved in PGH and Zn^{2+} binding (Lys-182 and His-178) (Fig. 6). The 227–237 loop undergoes substantial rearrangement, with the Pro-231 C$^{\alpha}$ atom position at the tip of the loop shifting 5.7 Å from its position in the ligand-free structure.

glFBPA PGH-Zn^{2+}-binding Sites—Zn^{2+} was not added to any of the solutions during protein purification and crystallization. Yet exposure of a crystal of the PGH-bound enzyme to synchrotron-tunable x-rays revealed a peak at 9674.2 eV corresponding to the absorption edge of zinc. Difference Fourier electron density maps show a bound ligand and Zn^{2+} in both molecules of the hexagonal crystal form and only in molecule A of the orthorhombic crystal form (Fig. 6*A*). The structures of the ligand-bound *gl*FBPA are the same in both crystal forms. Because the orthorhombic crystal form was determined at higher resolution (1.75 *versus* 2.3 Å), the analysis and the following discussion refer to the more accurately refined structure.

The *gl*FBPA active site is a highly polar cavity located at the C-terminal end of the β-strands of the barrel (Fig. 5), a feature shared with other α/β barrels (41). The active site environment is similar to that of the other class II aldolase family members of bacterial origin: *ec*FBPA (16), *ec*TBPA (20), and FBPA from *T. aquaticus* (37). The structures of *ec*FBPA and *ec*TBPA were determined in complex with the PGH inhibitor, and they are used here for the comparison with the structure of the *gl*FBPA active site. For convenience, the active site is subdivided into the Zn^{2+}, DHAP, and G3P sites. The DHAP site is occupied by the inhibitor PGH, whereas the G3P site is unoccupied, and its properties are inferred based on a model of a bound intact substrate.

Zn^{2+} Site—The bound Zn^{2+} has a trigonal bipyramidal coordination geometry similar to that seen in the crystal structures of *ec*TBPA and *ec*FBPA. Three Zn^{2+} ligands are provided by the N$^{\epsilon}$ atoms of His-84 and His-178, and the N$^{\delta}$ atom of His-210 (Fig. 6). The trigonal bipyramidal coordination is completed by the PGH N(OH) and C(1)O– groups. The distances between zinc-nitrogen and zinc-oxygen atoms are in the ranges of 2.1–2.3 and 2.5–2.6 Å, respectively. The exact positioning of two Zn^{2+} imidazole ligands, those of His-84 and His-210, are fixed by networks of electrostatic interactions as follows: the side chain of His-84 interacts with one of the oxygen atoms of the Asp-105 carboxylate group. The other oxygen atom interacts with the main chain nitrogen atom of Ser-107. The side chain of His-210 interacts with the carboxylate group of Glu-133. The electrostatic network is extended further by the Glu-133 side chain via its interaction with the side chains of His-81 and Lys-251. In contrast to these two well anchored histidine residues, the imidazole of His-178, located on one of the flexible loops (encompassing residues 174–194), is not involved in an extended network of interactions. It is possible that anchoring the position of His-178 through extensive electrostatic interactions might interfere with the order-disorder transition that the loop undergoes during catalysis.

The DHAP Site—The tight binding inhibitor PGH mimics the enediolate intermediate, which, in the ensuing step of catalysis, undergoes protonation to form DHAP (Fig. 2). The inhibitor binds in a deep polar cavity with the phosphate moiety stationed in a site enriched with the positive dipoles of four backbone amide groups (Gly-179, Ser-213, Asp-255, and Ser-256) (Fig. 6*B*). In addition, the phosphate group interacts with the amino group of Lys-182 on the 174–194 flexible loop and with the hydroxyl groups of Ser-213 and Ser-256. The phosphate-binding site is very similar to that present in *ec*FBPA and *ec*TBPA. An interesting difference between the bacterial aldolases and *gl*FBPA is that the monovalent cation that counters the phosphate negative charge in the bacterial aldolases is absent in *gl*FBPA. The cation is replaced by the ammonium substituent of the Lys-182 side chain. In addition to coordination with Zn^{2+}, the hydroxamate moiety of the PGH interacts with the backbone amide group of Gly-211, Asn-253, and Asp-83 (Fig. 6*B*). Asn-253 and Asp-83 are conserved in *ec*FBPA (numbered Asn-286 and Asp-109).

The G3P Site—The interaction of groups in *gl*FBPA with the G3P moiety was assessed by using a model of the enzyme-FBP complex (Fig. 7). In constructing this model, the PGH-binding mode was used to define the orientation of the DHAP-forming end of FBP and interactions with the G3P-forming end were optimized. Inspection of the model leads to the prediction that

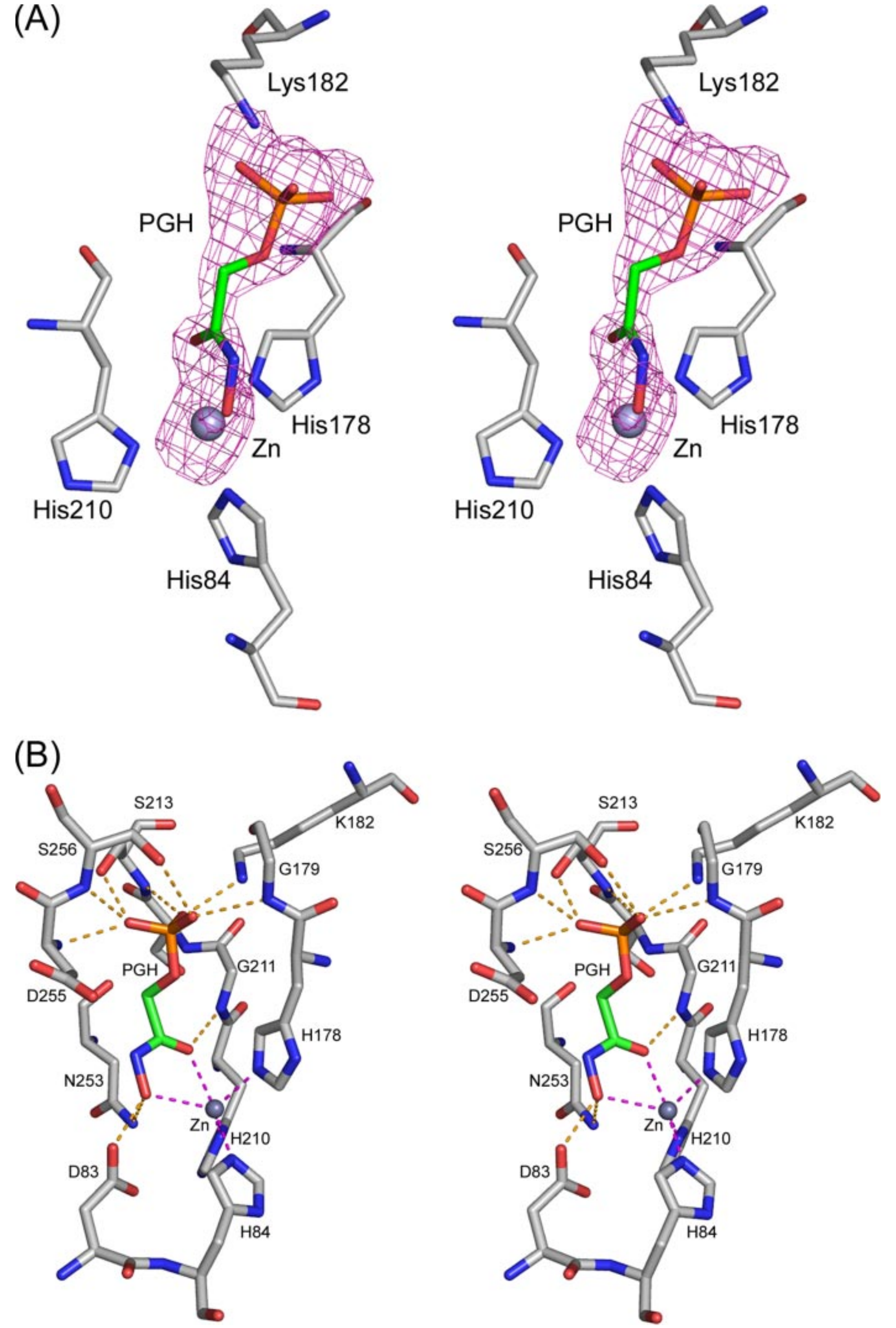

FIGURE 6. **Binding of PGH to *gl*FBPA.** *A,* stereoscopic view of the electron density in the vicinity of the active site. Difference electron density map with the coefficients $F_o - F_c$ was calculated prior to inclusion of the PGH ligand in the model. The map is countered at 3σ level. *B,* stereoscopic view of the environment of PGH. Atomic colors are as follows: oxygen, *red*; nitrogen, *blue*; carbon, *gray*; phosphor, *orange*; and zinc, *steel blue*. The carbon atoms of the PGH are colored in *green*. Key electrostatic interactions are shown as *dashed lines*.

Asp-83 binds the FBP through electrostatic interactions formed between the side chain carboxylate group and the substrate C(3) and C(4) hydroxyl groups. In addition, it suggests that Asp-83 functions to deprotonate the C(4) hydroxyl during catalytic turnover. To test this prediction, the D83A mutant was prepared and characterized. Although this mutant displays native protein behavior during purification, it does not have significant catalytic activity when subjected to forcing conditions (*viz.* 170 μM D83A FBPA with 2 mM FBP at pH 7.5 and 25 °C for 3 h). This condition defines a maximum turnover rate that is 5 orders of magnitude slower than the $k_{\text{cat}} = 3.55 \pm 0.05\ \text{s}^{-1}$ of the wild-type enzyme. The corresponding *ec*FBPA mutant D109A is also known to be catalytically impaired (17).

The properties of site-directed mutants of *ec*FBPA active site residues support the position of the G3P-forming end of the FBP. The studies indicate that Arg-331, Ser-61, Asp-288, and Asn-35 of the *E. coli* enzyme interact with the C(6) phosphate group and the C(4) and C(5) hydroxyl groups of FBP (17, 18, 42). Inspection of the *gl*FBPA-FBP model leads to the prediction that the FBP C(6) phosphate interacts with the Ser-50 hydroxyl, guanidinium group of Arg-259 and guanidinium group of Arg-280 (located on the opposing subunit). The observation that both subunits contribute to the active site interactions has been noted in earlier studies with *ec*FBPA, where the counterpart of Arg-280 is Arg-331 (42). In contrast, Arg-259 of *gl*FBPA does not have a counterpart in the *ec*FBPA. In *ec*FBPA this position is occupied by a glutamine (Gln-292). Consequently, it appears that the *gl*FBPA active site contains a more extensive charge network. Specifically, Arg-259 is anchored by the two carboxyl groups of Asp-255 and Asp-278 (the latter residing on the partner subunit), and in turn, Asp-278 interacts with Arg-280 (Fig. 7).

Interaction of the G3P phosphate group with the hydroxyl group of Ser-50 is conserved in the class II FBP aldolases (Ser-61 in *ec*FBPA). This is an important interaction as indicated by characterization of the S61A *ec*FBPA mutant (18).

In the *gl*FBPA-FBP model, the amide group of Asn-24 interacts with the G3P phosphate group as well as with the C(5) hydroxyl group of FBP. This is consistent with the observation that replacement of Asn-35, the corresponding residue in *ec*FBPA, by alanine results in impaired enzyme activity (17).

The *gl*FBPA-FBP-Zn^{2+} active site model described above serves two purposes. First, it provides a starting point for inhibitor design. Second, it provides insight into why TBP is not recognized as a substrate.

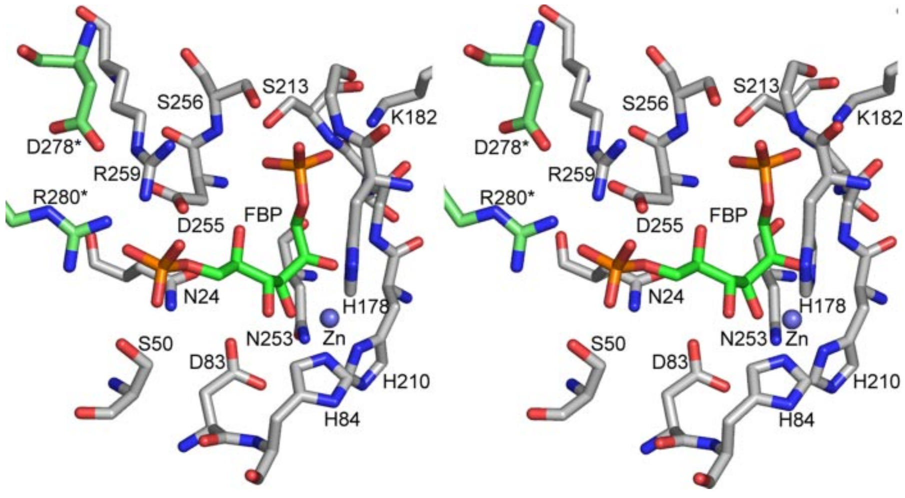

FIGURE 7. **Stereoscopic view of FBP modeled in the *gl*FBPA active site.** Atomic colors are the same as in Fig. 6. The carbon atoms of Arg-280 and Asp-278 from the partner subunit are colored in *light green* and indicated by *asterisk*.

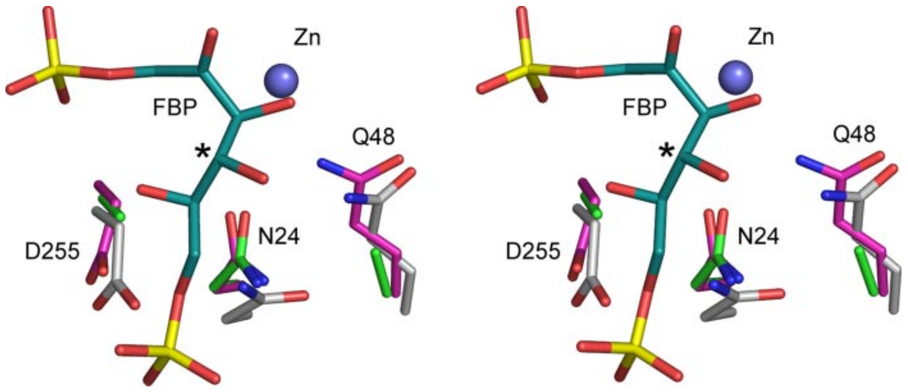

FIGURE 8. **Structural relationship between FBPAs and TBPA.** Stereoscopic view of superposed active site residues of *ec*FBPA (*gray carbon atoms*), *gl*FBPA (*magenta carbon atoms*), and *ec*TBPA (*green carbon atoms*) is shown. Other atomic colors are as follows: oxygen, *red*; nitrogen, *blue*; phosphor, *yellow*; and zinc, *steel blue*. The carbon atoms of FBP are colored in *cyan*. For clarity, only *gl*FBPA residues are labeled. The FBP C(4) position, the chirality of which distinguishes FBP from TBP, is indicated by an *asterisk*.

Aldolase II Substrate Specificity—The results of this study demonstrate that that TBP, the FBP C(4) hydroxyl epimer, binds tightly at the *gl*FBPA substrate site ($K_i = 2.4\ \mu\text{M}$), but it is not converted to products. As shown by Hunter and co-workers (20) (and demonstrated in Figs. 7 and 8), it is evident that if TBP binds to the *gl*FBPA active site in the same conformation as does FBP, the C(4) hydroxyl group would not be properly aligned for deprotonation by the Asp-83. Thus, from this perspective the basis for the stringent specificity is obvious. Because the TBPA aspartic acid that deprotonates the TBP C(4) hydroxyl is located in exactly the same position as Asp-83 in *gl*FBPA (Fig. 8), rotation about the C(3)–C(4) bond in TBP must occur in order to bring the C(4) hydroxyl close to the aspartic acid. However, the atoms beyond C(4) are forced into different spatial orientations with respect to the surrounding active site residues in this rotamer. This results in bad steric interactions with groups of both TBPA and FBPA (recall that the active site architecture of the two enzymes is very similar). To alleviate these clashes, additional bond rotation must take place, which could lead to nonproductive binding and no turnover.

In *E. coli* FBP and TBP are converted to G3P and DHAP by two different class II aldolases as follows: *ec*FBPA and *ec*TBPA. The *ec*FBPA substrate discrimination factor, expressed as $(k_{cat}/K_m(\text{FBP}))/(k_{cat}/K_m(\text{TBP}))$, was determined to be 1423 (18). The *ec*TBPA substrate discrimination factor, expressed as $(k_{cat}/K_m(\text{TBP}))/(k_{cat}/K_m(\text{FBP}))$, is 333. Although the substrate specificity is not as high in the two *E. coli* aldolases as it is in the *gl*FBPA, it is significant. Hunter and co-workers (20) identified Asp-288 and Gln-59 as residues that play an important role in discriminating between FBP and TBP substrates. In *gl*FBPA, Asp-288 corresponds to Asp-255 and Gln-59 corresponds to Gln-48. In *ec*TBPA, the positions of these two residues are occupied by alanine (Fig. 8). The fact that *gl*FBPA retains the "*ec*FBPA Asp-288" as Asp-255 is consistent with the substrate preference for FBP. Hunter and co-workers (20) suggested Gln-59 might influence the side-chain orientation of another conserved residue positioned to contact FBP, Asn-35 (Asn-24 in *ec*TBPA and Asn-24 in *gl*FBPA), and that the smaller alanine side chain leads to an alternate conformation of Asn-24 in TBPA. This conclusion is inconsistent with the observation that the active site arrangement of *gl*FBPA has Asn-24 oriented in a nearly identical manner as that observed for Asn-24 in *ec*TBPA. Moreover, site-directed mutagenesis experiments that attempted to "switch" specificity failed to provide a clear-cut answer (18).

Clearly, there must be other factors involved in determining substrate specificity. Additional studies (*e.g.* structure of an enzyme-substrate complex with an ordered active site loop) are required to gain better insight into this issue.

Conclusion—We have identified the key glycolytic cycle enzyme FBPA as a potential *Giardia* drug target. The *gl*FBPA, which belongs to the class II aldolase family, contrasts with the human FBPA that belongs to the evolutionarily unrelated class I aldolase family. We have shown that *Giardia* trophozoites produce this enzyme in the cytoplasm and that RNA silencing results in death of the parasite. Although both the amino acid sequence and crystal structure of *gl*FBPA are more similar to those of *ec*TBPA than *ec*FBPA (38 and 23% sequence identity, respectively), the kinetic characterization shows unequivocally that the true substrate is FBP and that its C(4) epimer, TBP, is a *gl*FBPA inhibitor. This finding underscores the importance of determining function experimentally rather than inferring it solely based on sequence/structure comparison.

REFERENCES

1. Adam, R. D. (2001) *Clin. Microbiol. Rev.* **14,** 447–475
2. Farthing, M. J. (1996) *Gastroenterol. Clin. North Am.* **25,** 493–515
3. Boreham, P. F., Phillips, R. E., and Shepherd, R. W. (1988) *Trans. R. Soc. Trop. Med. Hyg.* **82,** 104–106
4. Zaat, J. O., Mank, T. G., and Assendelft, W. J. (1997) *Trop. Med. Int. Health* **2,** 63–82
5. Upcroft, P., and Upcroft, J. A. (2001) *Clin. Microbiol. Rev.* **14,** 150–164
6. Wright, J. M., Dunn, L. A., Upcroft, P., and Upcroft, J. A. (2003) *Expert Opin. Drug Safety* **2,** 529–541
7. McArthur, A. G., Morrison, H. G., Nixon, J. E., Passamaneck, N. Q., Kim, U., Hinkle, G., Crocker, M. K., Holder, M. E., Farr, R., Reich, C. I., Olsen, G. E., Aley, S. B., Adam, R. D., Gillin, F. D., and Sogin, M. L. (2000) *FEMS Microbiol. Lett.* **189,** 271–273
8. Jarroll, E. L., Manning, P., Berrada, A., Hare, D., and Lindmark, D. G. (1989) *J. Protozool.* **36,** 190–197
9. Lindmark, D. G. (1980) *Mol. Biochem. Parasitol.* **1,** 1–12
10. Muller, M. (1988) *Annu. Rev. Microbiol.* **42,** 465–488
11. Henze, K., Morrison, H. G., Sogin, M. L., and Muller, M. (1998) *Gene* (*Amst.*) **222,** 163–168
12. Rutter, W. J. (1964) *Fed. Proc.* **23,** 1248–1257
13. Kobes, R. D., Simpson, R. T., Vallee, R. L., and Rutter, W. J. (1969) *Biochemistry* **8,** 585–588
14. Marsh, J. J., and Lebherz, H. G. (1992) *Trends Biochem. Sci.* **17,** 110–113
15. Cooper, S. J., Leonard, G. A., McSweeney, S. M., Thompson, A. W., Naismith, J. H., Qamar, S., Plater, A., Berry, A., and Hunter, W. N. (1996) *Structure* (*Lond.*) **4,** 1303–1315
16. Hall, D. R., Leonard, G. A., Reed, C. D., Watt, C. I., Berry, A., and Hunter, W. N. (1999) *J. Mol. Biol.* **287,** 383–394
17. Plater, A. R., Zgiby, S. M., Thomson, G. J., Qamar, S., Wharton, C. W., and Berry, A. (1999) *J. Mol. Biol.* **285,** 843–855
18. Zgiby, S. M., Thomson, G. J., Qamar, S., and Berry, A. (2000) *Eur. J. Biochem.* **267,** 1858–1868
19. Zgiby, S., Plater, A. R., Bates, M. A., Thomson, G. J., and Berry, A. (2002) *J. Mol. Biol.* **315,** 131–140
20. Hall, D. R., Bond, C. S., Leonard, G. A., Watt, C. I., Berry, A., and Hunter, W. N. (2002) *J. Biol. Chem.* **277,** 22018–22024
21. Keister, D. B. (1983) *Trans. R. Soc. Trop. Med. Hyg.* **77,** 487–488
22. Bradford, M. M. (1976) *Anal. Biochem.* **72,** 248–254
23. Collins, K. D. (1974) *J. Biol. Chem.* **249,** 136–142
24. Touz, M., Kulakova, T., and Nash, T. E. (2004) *Mol. Biol. Cell* **15,** 3053–3060
25. Otwinowski, Z., and Minor, W. (1997) *Methods Enzymol.* **276,** 307–326
26. Brünger, A. T., Adams, P. D., Clore, G. M., DeLano, W. L., Gros, P., Grosse-Kunstleve, R. W., Jiang, J. S., Kuszewski, J., Nilges, M., Pannu, N. S., Read, R. J., Rice, L. M., Simonson, T., and Warren, G. L. (1998) *Acta Crystallogr.* **54,** 905–921
27. Jones, T. A. (2004) *Acta Crystallogr.* **60,** 2115–2125
28. Laskowski, R. A., MacArthur, M. W., Moss, D. S., and Thornton, J. (1993) *J. Appl. Crystallogr.* **26,** 283–291
29. DeLano, W. L. (2002) *The PyMOL User's Manual*, DeLano Scientific, San Carlos, CA
30. Mills, S. D. (2003) *J. Antimicrob. Chemother.* **51,** 749–752
31. Projan, S. J. (2002) *Curr. Opin. Pharmacol.* **2,** 513–522
32. Giaever, G., Chu, A. M., Ni, L., Connelly, C., Riles, L., Veronneau, S., Dow, S., Lucau-Danila, A., Anderson, K., Andre, B., Arkin, A. P., Astromoff, A., El-Bakkoury, M., Bangham, R., Benito, R., Brachat, S., Campanaro, S., Curtiss, M., Davis, K., Deutschbauer, A., Entian, K. D., Flaherty, P., Foury, F., Garfinkel, D. J., Gerstein, M., Gotte, D., Guldener, U., Hegemann, J. H., Hempel, S., Herman, Z., Jaramillo, D. F., Kelly, D. E., Kelly, S. L., Kotter, P., LaBonte, D., Lamb, D. C., Lan, N., Liang, H., Liao, H., Liu, L., Luo, C., Lussier, M., Mao, R., Menard, P., Ooi, S. L., Revuelta, J. L., Roberts, C. J., Rose, M., Ross-Macdonald, P., Scherens, B., Schimmack, G., Shafer, B., Shoemaker, D. D., Sookhai-Mahadeo, S., Storms, R. K., Strathern, J. N., Valle, G., Voet, M., Volckaert, G., Wang, C. Y., Ward, T. R., Wilhelmy, J., Winzeler, E. A., Yang, Y., Yen, G., Youngman, E., Yu, K., Bussey, H., Boeke, J. D., Snyder, M., Philippsen, P., Davis, R. W., and Johnston, M. (2002) *Nature* **418,** 387–391
33. Altschul, S. F., Madden, T. L., Schaffer, A. A., Zhang, J., Zhang, Z., Miller, W., and Lipman, D. J. (1997) *Nucleic Acids Res.* **25,** 3389–3402
34. Dobeli, H., Itin, C., Meier, B., and Certa, U. (1991) *Acta Leiden.* **60,** 135–140
35. Bakker, B. M., Westerhoff, H. V., Opperdoes, F. R., and Michels, P. A. (2000) *Mol Biochem. Parasitol.* **106,** 1–10
36. Ramsaywak, P. C., Labbe, G., Siemann, S., Dmitrienko, G. I., and Guillemette, J. G. (2004) *Protein Expression Purif.* **37,** 220–228
37. Izard, T., and Sygusch, J. (2004) *J. Biol. Chem.* **279,** 11825–11833
38. Schomburg, I., Chang, A., Ebeling, C., Gremse, M., Heldt, C., Huhn, G., and Schomburg, D. (2004) *Nucleic Acids Res.* **32,** D431–D433
39. Bernstein, E., Denli, A. M., and Hannon, G. J. (2001) *RNA* (*Cold Spring Harbor*) **7,** 1509–1521
40. Sun, C. H., and Tai, J. H. (2000) *Mol. Biochem. Parasitol.* **105,** 51–60
41. Brändén, C.-I. (1980) *Q. Rev. Biophys.* **13,** 317–338
42. Qamar, S., Marsh, K., and Berry, A. (1996) *Protein Sci.* **5,** 154–161